Forces and torques on a sphere moving near a dihedral corner in creeping flow

F. Romanò [a,b,*], P.-E. des Boscs [c], H.C. Kuhlmann [c]

[a] Univ. Lille, CNRS, ONERA, Arts et Métiers, Centrale Lille, FRE 2017-LMFL-Laboratoire de Mécanique des Fluides de Lille - Kampé de Fériet, F-59000, Lille, France
[b] Department of Biomedical Engineering, University of Michigan, 2200 Bonisteel Boulevard, Ann Arbor, MI 48109, USA
[c] Institute of Fluid Mechanics and Heat Transfer, TU Wien, Getreidemarkt 9, 1060 Vienna, Austria

A B S T R A C T

The low-Reynolds-number flow past a sphere moving near a right dihedral corner made by a stationary and a tangentially sliding wall is considered. Using the superposition principle, the arbitrary motion of the sphere is decomposed into simple elementary motions. Fully-resolved spectral-element simulations are carried out in the frame of reference translating and rotating with the particle such that the velocity on the particle's surface vanishes. Forces and torques on the sphere are obtained as functions of the particle position near the corner. The data obtained are fitted by closed-form expressions which take into account symmetries of the problem, exact solutions, and asymptotic solutions from lubrication theory. The correlations obtained can easily be implemented in larger-scale one-way-coupled particulate-flow simulations to correct the particle motion near dihedral corners where mere point-particle models break down.

1. Introduction

The presence of rigid indeformable boundaries strongly affects the hydrodynamic forces and torques exerted by a fluid on a particle moving near a wall, a free-surface, or other particles or bubbles. This situation is found for sedimenting and resuspending particles [1], transport of particles along rivers [2], and particulate combustion and sprays [3]. Lubrication forces between particle and boundary become increasingly important in small-scale confined flows, e.g. in microfluidic applications, and can lead to coherent particle structures [4–7].

Several studies have considered the low-Reynolds-number flow past a spherical particle and the hydrodynamic forces and torques acting when it moves near a wall, a free surface, or another particle. Lorentz [8] theoretically investigated a sphere moving towards a plane rigid wall when the distance between the particle centroid and the wall is much larger than the radius of the sphere. The axisymmetric problem of a sphere with fixed centroid rotating about the principal axis perpendicular to a nearby plane wall was solved by Jeffery [9]. Stimson & Jeffery [10] considered the case of two non-rotating spheres approaching each other along the line connecting their centroids in an infinitely extended fluid domain. A recent extension of their solution is due to Papavassiliou & Alexander [11]. Improving the Stokes-flow result, Faxén [12] obtained an approximate solution for a sphere moving parallel to a rigid wall using the Oseen approximation. These studies were complemented by Brenner [13], who provided the solution for the problem of a sphere moving towards an indeformable plane rigid wall or a free surface in creeping flow. Dean & O'Neill [14] and O'Neill & Stewartson [15] investigated the slow steady flow near a plane wall due to a sphere rotating about an arbitrary axis and translating in direction parallel to the wall. The solution given by Dean & O'Neill [14] for a rotating sphere was subsequently corrected by Goldman et al. [16], who computed hydrodynamic forces and torques in the two limits of a vanishing lubrication gap and of a large distance between the particle and the wall. For creeping flow they demonstrated, furthermore, that a sphere subject to gravitational forces rolls down an inclined plane without any physical contact. Goldman et al. [17] considered a neutrally-buoyant sphere of radius a in a shear flow near a plane wall for (a) vanishingly small lubrication gap $\delta \ll a$ between the sphere and the wall, and (b) for a sphere far from the wall such that $\delta = \mathcal{O}(a)$. Other theoretical investigations have been carried out by Haberman & Sayre [18] and Sonshine et al. [19], who investigated the effect of boundaries on a particle immersed in a cylindrical tank. Cox & Brenner [20] included inertial effects in the solution of Brenner [13], and Bart [21] solved the unsteady problem of a sphere moving towards an indeformable interface between two immiscible fluids. The latter work was extended by Lee & Leal [22]

* Corresponding author at: Department of Biomedical Engineering, University of Michigan, 2200 Bonisteel Boulevard, Ann Arbor, MI 48109, USA.
E-mail address: francesco.romano@ensam.eu (F. Romanò).

and Geller et al. [23] who studied the motion of a sphere rising towards an interface which can either be rigid or deformable. Corresponding measurements [21,24] confirmed the theoretical predictions made for low-Reynolds-number flows. Reviews of these theoretical and experimental results can be found in [22] and [25].

The result obtained for Stokes flow have been extended by Cox & Mason [26] by taking into account inertial flow effects when a sphere moves in a confined rotational flow. More recently, Liu & Prosperetti [27] investigated the inertial flow past a sphere rotating near a wall, between two parallel walls, or inside a concentric cube. Other investigations extended the results for creeping Newtonian flow to other rheologies. Kim & Russel [28] investigated the hydrodynamic interaction between two spheres in a Brinkman medium, and Damiano et al. [29] focused on particles immersed in or moving near a Brinkman medium.

The attention paid to particle–boundary interaction models is further motivated by a number of problems where modeling the boundary-induced repulsion is crucial for performing predictive simulations. This is the case, for instance, when two-dimensional limit cycles [30–32] and finite-size Lagrangian coherent structures are created by the particle–boundary interaction which focuses finite-size particles in regular regions of the flow near the boundaries [33]. These phenomena have been experimentally observed first in thermocapillary liquid bridges [4,34] and recently numerically reproduced and theoretically explained by [6, 35–38]. For an overview on finite-size coherent structures in liquid bridges, we refer to [39]. The same particle accumulation phenomenon has been experimentally observed and numerically reproduced in mechanically-driven systems, such as a lid-driven cavity [7,40,41]. As pointed out by [7], spurious particle attractors are found using the current simplified particle–boundary interaction models which are based on phenomenological approaches [35] or on classic lubrication models [7]. Within this framework, our study aims at introducing corner-flow corrections that are believed to be the source of the spurious attractors observed in numerical simulations, but were never reported in experiments.

Related to the present work, Dauparas & Lauga [42] analytically investigated the leading-order force and torque on a sphere in creeping flow at a distance $\delta \gg a$ from a steady dihedral corner. In our paper, we rather consider the case of a sphere in creeping flow moving near ($\delta = \mathcal{O}(a)$) a right dihedral corner formed by a steady and a tangentially sliding wall. We are interested in the dependence of the forces and torques on the position of the sphere in order to derive correlations which could be used in larger-scale numerical simulations to correct for boundary and edge effects [7,43]. In Section 2 the mathematical problem is formulated. Section 3 presents the numerical method used to simulate the Stokes flow past the particle. The results obtained are presented in Section 4, and in Section 5 the results are summarized and conclusions are drawn.

2. Problem formulation

A rigid spherical particle is moving near a semi-infinite dihedral edge in an incompressible Newtonian fluid of density ρ and kinematic viscosity ν (Fig. 1). Using Cartesian coordinates (x, y, z), the edge is formed by two orthogonal plane walls which meet at $\boldsymbol{x} = (0, y, 0)$. While the wall at $x = 0$ is stationary, the wall at $z = 0$ moves tangentially in its own plane with a constant velocity $\boldsymbol{U}_\mathrm{w} = (U_\mathrm{w}, V_\mathrm{w}, 0)$. We are interested in the forces on a spherical particle with radius a which translates with velocity $\boldsymbol{U} = (U, V, W)$ and rotates with angular velocity $\boldsymbol{\Omega} = (\Omega_x, \Omega_y, \Omega_z)$.

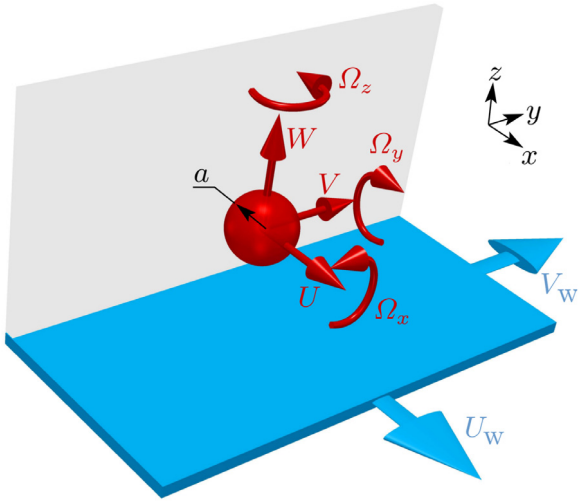

Fig. 1. Sketch of the sphere in creeping flow near a semi-infinite dihedral corner made by a stationary (light gray) and a moving wall (light blue) at 90°. The arrows indicate the possible translational and rotational motions. (For interpretation of the references to color in this figure legend, the reader is referred to the web version of this article.)

The motion of the fluid around the sphere is governed by the Navier–Stokes and continuity equations

$$\partial_t \boldsymbol{u} + \boldsymbol{u} \cdot \nabla \boldsymbol{u} = -\frac{1}{\rho}\nabla p + \nu \nabla^2 \boldsymbol{u}, \tag{1a}$$

$$\nabla \cdot \boldsymbol{u} = 0, \tag{1b}$$

where $\boldsymbol{u}(\boldsymbol{x}, t)$ and $p(\boldsymbol{x}, t)$ denote the velocity and pressure field, respectively. No-slip and no-penetration boundary conditions are imposed on the plane walls

$$x = 0: \quad \boldsymbol{u} = \boldsymbol{0}, \tag{2a}$$

$$z = 0: \quad \boldsymbol{u} = \boldsymbol{U}_\mathrm{w}. \tag{2b}$$

In the presence of a spherical particle no-slip and no-penetration boundary conditions must hold on the particle's surface

$$\boldsymbol{x} = \boldsymbol{x}_\mathrm{s}: \quad \boldsymbol{u} = \boldsymbol{U} + \boldsymbol{\Omega} \times (\boldsymbol{x}_s - \boldsymbol{x}_p), \tag{3}$$

where $\boldsymbol{x}_\mathrm{s}$ and $\boldsymbol{x}_p = (x_p, 0, z_p)$ describe the surface and the centroid of the sphere, respectively.

In the simultaneous limits of a small wall Reynolds number $\mathrm{Re} = |\boldsymbol{U}_\mathrm{w}|L/\nu \ll 1$, where L is the characteristic length of the global fluid flow, and a small particle Reynolds number $\mathrm{Re}_\mathrm{p} = |\boldsymbol{U} + \boldsymbol{\Omega} \times (\boldsymbol{x}_s - \boldsymbol{x}_p) - \boldsymbol{u}|a/\nu \ll 1$, the material derivative can be neglected with respect to the viscous term and (1a) reduces to a balance between pressure and viscous forces, leading to the Stokes-flow approximation. Using the scalings a, ν/a and $\rho\nu^2/a^2$, for length, velocity and pressure, respectively, the dimensionless momentum equation becomes

$$\nabla p = \nabla^2 \boldsymbol{u}. \tag{4}$$

On the remaining boundaries at a large distance of order $O(\lambda = L/a)$ from the particle, with $|\boldsymbol{x}_p| \ll \lambda$, we assume that flow perturbations due to the presence of the particle are small, while the flow due to the moving wall is still creeping ($\mathrm{Re} \ll 1$), i.e. $\lambda \ll \nu/(|\boldsymbol{U}_W|a)$. Under this assumption the two-dimensional velocity field far from the particle is given by [44]

$$|\boldsymbol{x}| = O(\lambda): \quad u = U_\mathrm{w}\left[f'(\theta)\cos(\theta) + f(\theta)\sin(\theta)\right], \tag{5a}$$

$$v = V_\mathrm{w}(1 - 2\theta/\pi), \tag{5b}$$

$$w = U_\mathrm{w}\left[f'(\theta)\sin(\theta) - f(\theta)\cos(\theta)\right], \tag{5c}$$

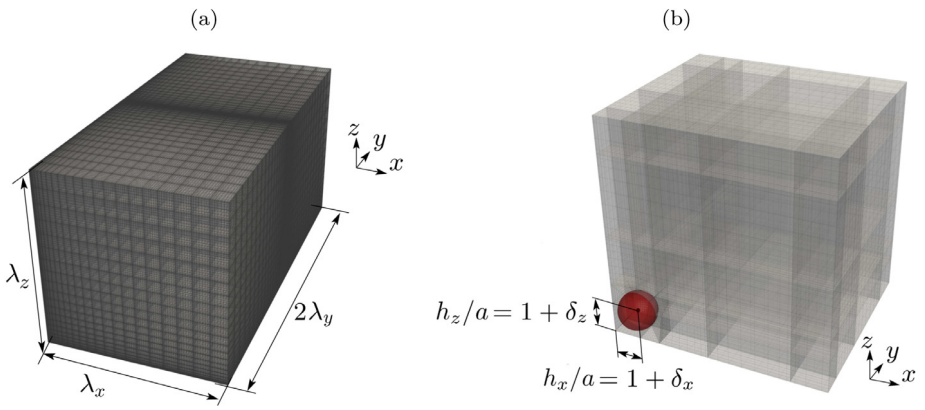

Fig. 2. (a) Distribution of the elements within the whole computational domain. (b) Zoom into the region near the particle. The spectral elements are fitted to the spherical shape of the particle (red). (For interpretation of the references to color in this figure legend, the reader is referred to the web version of this article.)

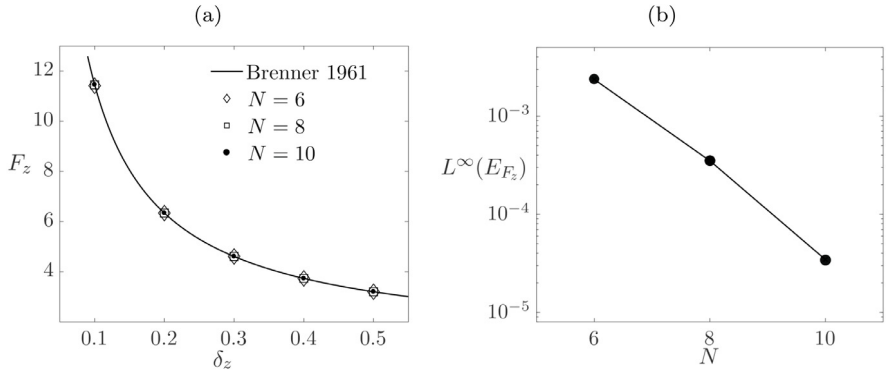

Fig. 3. (a) Comparison between the numerical simulations (markers) and the analytic solution of Brenner [13] (line) for the wall-normal drag on a particle moving towards a plane wall. (b) Spectral convergence in infinite norm of the numerical error (difference between computational and exact solution [13]) obtained considering three polynomial degrees, i.e. $N = 6$, 8 and 10.

where $f(\theta) = [\theta \sin(\pi/2 - \theta) - \pi/2(\pi/2 - \theta)\sin\theta]/(1 - \pi^2/4)$ and $\theta = \cos^{-1}\left(x/\sqrt{x^2 + z^2}\right)$.

The quasi-steady approximation employed does not carry any memory from previous times. Therefore, the flow field depends only on the instantaneous configuration. Since the Stokes equation (4) is linear, the superposition principle allows to obtain the solution as a linear combination of solutions to the following elementary sub-problems (and their symmetric counterparts) with suitably defined far-field conditions.

(I) A sphere moving parallel to the edge made by two stationary walls

$$\boldsymbol{U}_w = \boldsymbol{0}, \quad \boldsymbol{U} = \boldsymbol{e}_y, \quad \boldsymbol{\Omega} = \boldsymbol{0}, \tag{6}$$

(II) a sphere rotating about an axis parallel to the edge made by two stationary walls

$$\boldsymbol{U}_w = \boldsymbol{0}, \quad \boldsymbol{U} = \boldsymbol{0}, \quad \boldsymbol{\Omega} = \boldsymbol{e}_y, \tag{7}$$

(III) a sphere moving normal to one wall with both walls stationary

$$\boldsymbol{U}_w = \boldsymbol{0}, \quad \boldsymbol{U} = \boldsymbol{e}_x, \quad \boldsymbol{\Omega} = \boldsymbol{0}, \tag{8}$$

(IV) a sphere rotating about an axis normal to one wall with both walls stationary

$$\boldsymbol{U}_w = \boldsymbol{0}, \quad \boldsymbol{U} = \boldsymbol{0}, \quad \boldsymbol{\Omega} = \boldsymbol{e}_z, \tag{9}$$

(V) a steady sphere near a dihedral corner with one wall moving parallel to the edge

$$\boldsymbol{U}_w = \boldsymbol{e}_y, \quad \boldsymbol{U} = \boldsymbol{0}, \quad \boldsymbol{\Omega} = \boldsymbol{0}, \tag{10}$$

(VI) a steady sphere near a dihedral corner with one wall moving normal to the edge

$$\boldsymbol{U}_w = \boldsymbol{e}_x, \quad \boldsymbol{U} = \boldsymbol{0}, \quad \boldsymbol{\Omega} = \boldsymbol{0}. \tag{11}$$

All the six fundamental problems are solved in the frame of reference translating and rotating with the particle. Hence, the particle's surface is at rest in the computational frame. To take this transformation into account, the boundary conditions for the fluid on the two walls are obtained by subtracting the velocity due to the transformation to the co-moving frame of reference from (2), i.e. from the velocities the boundaries would have in the laboratory frame.

3. Numerical method

The problem (4) is discretized using a spectral-element method, making use of a nodal approach based on Lagrange polynomials defined on Gauss–Legendre–Lobatto nodes. The functional spaces for velocity and pressure are selected in respect of the inf–sup condition, i.e. the couple $(\boldsymbol{u}, p)$ belongs to the polynomial spaces $\mathbb{P}^N - \mathbb{P}^{N-2}$. The 3/2 over-integration rule is always employed in order to cure aliasing errors which arise computing by Gauss quadrature the integrals of our Galerkin weak formulation.

The Stokes solver implemented in the open-source software Nek5000 is used to carry out the computations. The rectangular computational domain is $[0, \lambda_x] \times [-\lambda_y, \lambda_y] \times [0, \lambda_z]$ with $\lambda_{x,y,z} = 360$. The centroid of the sphere is placed in the midplane at $(x_p, y_p, z_p) = (1 + \delta_x, 0, 1 + \delta_z)$ (see Fig. 2). Since the distance of the sphere's centroid from any wall is always less than two,

Table 1
p-convergence: non-zero forces and torques on a sphere at $(x_p, z_p) = (1.1, 1.1)$ as functions of the polynomial order N. The relative errors E are defined with respect to the finest grid, e.g. $E_{F_x} = |(F_x|_N - F_x|_{N=12})/F_x|_{N=12}|$.

Problem I						
N	F_y	T_x	T_z	E_{F_y}	E_{T_x}	E_{T_z}
6	3.418544	−0.0098827	0.0098827	0.0001480	0.1521217	0.1521217
8	3.417875	−0.0115779	0.0115779	0.0000477	0.0066834	0.0066834
10	3.418033	−0.0116524	0.0116524	0.0000015	0.0002917	0.0002917
12	3.418038	−0.0116558	0.0116558			
Problem II						
N	F_x	F_z	T_y	E_{F_x}	E_{F_z}	E_{T_y}
6	−0.071339	0.071339	−1.7666238	0.0223650	0.0223650	0.0011169
8	−0.072770	0.072770	−1.7685391	0.0027545	0.0027545	0.0000340
10	−0.072934	0.079434	−1.7685957	0.0005070	0.0005070	0.0000020
12	−0.072971	0.072971	−1.7685992			
Problem III						
N	F_x	F_z	T_y	E_{F_x}	E_{F_z}	E_{T_y}
6	−13.84389	−2.049813	−0.0538792	0.0066674	0.0052042	0.0432627
8	−13.93053	−2.060257	−0.0562527	0.0004509	0.0001357	0.0011165
10	−13.93674	−2.060521	−0.0563166	0.0000051	0.0000076	0.0000189
12	−13.93681	−2.060537	−0.0563155			
Problem IV						
N	F_y	T_x	T_z	E_{F_y}	E_{T_x}	E_{T_z}
6	−0.014870	0.023849	−1.5374589	0.0260676	0.0111534	0.0009692
8	−0.015098	0.024108	−1.5389064	0.0111344	0.0004146	0.0000286
10	−0.015214	0.024117	−1.5389483	0.0035368	0.0000415	0.0000014
12	−0.015268	0.024118	−1.5389505			
Problem V						
N	F_y	T_x	T_z	E_{F_y}	E_{T_x}	E_{T_z}
6	1.813707	−0.181522	−0.1799225	0.0008724	0.0056858	0.0121488
8	1.812684	−0.182242	−0.1781167	0.0003079	0.0017419	0.0019903
10	1.812077	−0.182509	−0.1776767	0.0000270	0.0002794	0.0004849
12	1.812126	−0.182560	−0.1777629			
Problem VI						
N	F_x	F_z	T_y	E_{F_x}	E_{F_z}	E_{T_y}
6	1.358695	−0.209206	0.2735443	0.0661762	0.9844624	0.0050905
8	1.423157	−0.141202	0.2749107	0.0218718	0.3393978	0.0001207
10	1.451972	−0.113675	0.2749414	0.0020674	0.0782854	0.0000091
12	1.454980	−0.109422	0.2749439			

e.g. $x_p \leq 2$, the computational domain is large compared to the particle's radius and compared to its distance from the walls. Therefore, the flow due to the presence of the sphere is negligibly small on the far domain boundaries, and the unperturbed Stokes flow (5a)–(5c) can be imposed on the boundaries at $x = \lambda_x$, $y = \pm\lambda_y$ and $z = \lambda_z$.

The spectral element grid consists of 20344 elements, which corresponds to 15021380 degrees of freedom. A body-fitted mesh is used to represent the sphere. Close to the sphere, the elements are slightly deformed in order to allocate an ad-hoc h-refinement of the mesh around the surface of the sphere. Since the Stokes problem is time-independent, the computational grid is stationary. A typical computational mesh is shown in Fig. 2, depicting the global computational domain (a) and a zoom towards the particle (b). Forces and torques exerted by the fluid on the particle are computed integrating the stresses over the spherical surface by Gaussian quadrature with the 3/2 over-integration rule.

4. Results

4.1. Validation

To validate the numerical code a comparison is made with the exact solution of Brenner [13] for a particle moving towards a wall in creeping flow. In this setting, the force on the particle is always directed normal to the wall. To carry out the computations for this test problem the wall at $x = 0$ is removed and the grid shown in Fig. 2 is mirrored with respect to the $(x = 0)-$plane. A particle moving with velocity $\boldsymbol{U} = (0, 0, -1)$ is placed at $(x_p, y_p, z_p) = (0, 0, 1 + \delta_z)$. Fig. 3(a) shows the computed wall-normal forces scaled by the Stokes drag $(6\pi\rho\nu a|U|)$ F_z for five different values of δ_z and and for polynomial orders $N = 6$, 8 and 10. The corresponding p-convergence is depicted in Fig. 3(b). The agreement between the numerical and the exact solution is excellent.

The convergence of the forces and torques on a sphere for the corner-flow problem under consideration is investigated for $\delta_x = \delta_z = 0.1$. Keeping constant the distribution of the spectral elements, a p-convergence study is carried out. Table 1 demonstrates that the forces and torques on the sphere exhibit convergence up to several digits when the polynomial order is $N = 10$ (15^3 Gauss nodes are used for the over-integration). Based on these results the polynomial order $N = 10$ is used for all subsequent computations.

4.2. Fundamental results of lubrication theory and exact solutions

In the limit of vanishing distance $\delta := \delta_x \to 0$ of the sphere from a plane wall and with $\delta_z \to \infty$, or vice versa, the asymptotic form of the forces and torques is known from lubrication theory. Since the numerical simulations must be compatible with the asymptotic results and reproduce known exact solutions, these are briefly summarized. Let $\boldsymbol{n}$ be the wall-normal unit vector and $(\boldsymbol{t}_1\boldsymbol{t}_2)$ the two tangent unit vectors on the plane, such that the

Table 2
Fit coefficients for the non-zero forces and torques acting on a sphere according to (13).

	Case I			Case II			Case III		
	F_y	T_x	T_z	F_x	F_z	T_y	F_x	F_z	T_y
A_1	−0.3798	$\alpha_{T_x}=0$	−0.0162	$\alpha_{F_x}=0$	−0.1639	−1.7510	−1.5646	$\alpha_{F_z}=0$	$\alpha_{T_y}=0$
A_2	−2.4726	$\alpha_{T_x}=0$	−14.5643	$\alpha_{F_x}=0$	−19.9627	−2.2417	−6.7898	$\alpha_{F_z}=0$	$\alpha_{T_y}=0$
A_3	−0.3798	−0.0162	$\beta_{T_z}=0$	−0.1639	$\beta_{F_z}=0$	−1.7510	−0.2599	$\beta_{F_z}=0$	−0.0605
A_4	−2.4726	−14.5643	$\beta_{T_z}=0$	−19.9627	$\beta_{F_z}=0$	−2.2417	−37.6495	$\beta_{F_z}=0$	−10.8926
B_1	−2.0025	−4.7384	4.7384	−26.4643	26.4643	−0.6718	−4.4088	−5.6664	14.1699
B_2	−0.0830	−0.7895	−0.7895	−2.6278	−4.4123	−0.1006	−12.0391	−2.3672	−1.3375
B_3	−0.0830	−1.9566	−1.9566	−4.4123	−2.6278	−0.1006	−1.6057	−1.0773	−3.6786
B_4	−0.1253	0.0023	0.0023	2.0424	1.2880	1.0485	−0.5482	1.7676	1.3015
B_5	−0.1253	−0.1228	−0.1228	1.2880	2.0424	1.0485	0.0072	0.5239	−0.0002
C_1	0.7600	−10.5132	−15.1638	−3.1747	−0.3929	−0.4830	−10.0331	−4.8746	−13.4879
C_2	−0.2400	−0.9493	−1.8691	−4.2052	−1.7985	−0.4962	−1.4504	−3.2699	−1.2928
C_3	−0.8978	−1.8491	−0.8966	−3.8579	−0.6559	−1.7478	−1.7173	−1.9287	−3.3980
C_4	0.8205	−0.0010	−0.0441	1.0873	0.7768	−0.2752	1.4786	0.2711	1.2118
D_1	0.7600	15.1638	10.5132	0.3929	3.1747	−0.4830	−10.3575	−6.1101	0.6635
D_2	−0.8978	−0.8966	−1.8491	−0.6559	−3.8579	−1.7478	−2.8118	−9.8853	−0.9036
D_3	−0.2400	−1.8691	−0.9493	−1.7985	−4.2052	−0.4962	−1.5570	−7.6463	−2.4932
D_4	0.8205	−0.0441	−0.0010	0.7768	1.0873	−0.2752	−0.0841	0.3376	1.1230
	Case IV			Case V			Case VI		
	F_y	T_x	T_z	F_y	T_x	T_z	F_x	F_z	T_y
A_1	−0.9534	$\alpha_{T_x}=0$	−0.2440	$\alpha_{F_y}=0$	$\alpha_{T_x}=0$	$\alpha_{T_z}=0$	$\alpha_{F_x}=0$	$\alpha_{F_z}=0$	$\alpha_{T_y}=0$
A_2	−4.0844	$\alpha_{T_x}=0$	−0.7313	$\alpha_{F_y}=0$	$\alpha_{T_x}=0$	$\alpha_{T_z}=0$	$\alpha_{F_x}=0$	$\alpha_{F_z}=0$	$\alpha_{T_y}=0$
A_3	$\beta_{F_y}=0$	$\beta_{T_x}=0$	−2.8383	−0.2617	−0.0633	$\beta_{T_z}=0$	−14.3738	$\beta_{F_z}=0$	−168.5633
A_4	$\beta_{F_y}=0$	$\beta_{T_x}=0$	−18.2681	−6.9855	−29.6632	$\beta_{T_z}=0$	−69.1733	$\beta_{F_z}=0$	−17.9721
B_1	0.5263	0.0752	1.6865	11.2238	0.4280	−0.1713	−3.3308	−2.5759	−0.5380
B_2	−0.5309	−2.5308	0	−0.1705	−0.1666	−0.7235	−1.4017	−0.7410	−0.6218
B_3	−0.9471	−1.2985	−6.8690	−3.5914	−0.7726	−0.0256	−0.1523	−1.1929	−0.0081
B_4	0.9284	1.6340	−1.7860	−0.0162	0.9248	0.2095	1.1946	0.8067	0.8673
B_5	1.7859	0.3857	10.7261	1.3963	−0.0638	−0.1034	−0.0963	1.7156	0.2501
C_1	0.0020	0.0508	−1.1319	2.5034	6.3211	0.0809	−10.3448	8.4908	−1.5388
C_2	−1.0717	−3.3257	−2.5221	−0.2480	−0.2204	−0.5292	−4.9219	−4.9481	−4.6636
C_3	−0.7929	−1.9897	−0.2702	−5.6273	−1.0754	−4.3201	−0.9479	−5.6816	−3.7982
C_4	−1.4025	0.1478	−0.1645	−0.0132	−0.0010	0.8472	0.7057	2.2431	1.7595
D_1	−0.0915	0.0287	−0.8108	5.1687	−6.2823	−0.1675	−1.7035	−1.8089	−0.7581
D_2	−1.2408	−9.9228	−7.8318	−0.0191	−0.1466	−3.7283	−0.3082	−0.9703	−0.4309
D_3	−2.1431	−8.1499	−0.3186	−2.6056	−1.0967	−1.5895	−1.4688	−0.7462	−6.3617
D_4	0.0159	0.2820	2.6567	3.5427	0.0083	0.1890	0.7932	0.0175	0.4302

system formed by $(\boldsymbol{t}_1, \boldsymbol{t}_2, \boldsymbol{n})$ is right handed, the asymptotic forms (12b) and (12d) by Chaoui & Feuillebois [45] and the exact solutions (12a) and (12c) by Brenner [13] and Jeffery [9], respectively, hold for a particle translating or rotating near a stationary wall

$$\boldsymbol{U}\cdot\boldsymbol{n}=1:\quad \boldsymbol{F}\cdot\boldsymbol{n}=\frac{4}{3}\sinh\gamma\sum_{n=1}^{\infty}\frac{n\,(n+1)}{(2n-1)\,(2n+3)}\left\{\frac{2\sinh\left[(2n+1)\gamma\right]+(2n+1)\sinh\left(2\gamma\right)}{4\sinh^2\left[(n+1/2)\gamma\right]-(2n+1)^2\sinh^2\gamma}-1\right\} \tag{12a}$$

$$\boldsymbol{U}\cdot\boldsymbol{t}_1=1:\quad \begin{aligned}\boldsymbol{F}\cdot\boldsymbol{t}_1&=8/15\log(\delta)+64/375\delta\log(\delta)-0.9543+\cdots\\ \boldsymbol{T}\cdot\boldsymbol{t}_2&=-1/10\log(\delta)-43/250\delta\log(\delta)-0.1929+\cdots\end{aligned} \tag{12b}$$

$$\boldsymbol{\Omega}\cdot\boldsymbol{n}=1:\quad \boldsymbol{T}\cdot\boldsymbol{n}=\sum_{n=0}^{\infty}\frac{\sinh^3(\gamma)}{\sinh^3\left[\gamma\,(n+1)\right]} \tag{12c}$$

$$\boldsymbol{\Omega}\cdot\boldsymbol{t}_2=1:\quad \begin{aligned}\boldsymbol{F}\cdot\boldsymbol{t}_1&=-2/15\log(\delta)-0.2526+\cdots,\\ \boldsymbol{T}\cdot\boldsymbol{t}_2&=2/5\log(\delta)+0.5280\delta\log(\delta)-0.3709+\cdots,\end{aligned} \tag{12d}$$

where $\gamma=\cosh^{-1}(\delta)$. The force $\boldsymbol{F}$ and the torque $\boldsymbol{T}$ exerted by the fluid on the sphere are scaled, respectively, by the drag $F^*=6\pi\rho\nu aU$ and the couple $T^*=8\pi\rho\nu a^2U$ in the unbounded domain with U the velocity of the wall or the particle's surface, i.e. $|\boldsymbol{U}|$, $|\boldsymbol{U}_w|$ or $a|\boldsymbol{\Omega}|$. All drag and couple components not listed in (12) vanish.

4.3. Fit functions

Steady flows for all six fundamental cases defined in Section 2 are calculated numerically for a 10×10 evenly-spaced grid of particle locations $(\delta_x,\delta_z)\in[0.1,1]^2$. The non-zero hydrodynamic forces and torques on the particle obtained are shown by markers in Fig. 4. To provide the forces and torques in a functional form which could be employed in Lagrangian particle tracking where the position of the particle centroid is not known a priori the numerical data are fitted (lines in Fig. 4) by

$$\begin{aligned}\boldsymbol{F}(\delta_x,\delta_z),\boldsymbol{T}(\delta_x,\delta_z)=\;&\alpha_*(\delta_x)(1-e^{A_1\delta_z})(1-e^{2A_2\theta/\pi})+\\ &\beta_*(\delta_z)(1-e^{A_3\delta_x})(1-e^{A_4(1-2\theta/\pi)})+\\ &B_1e^{B_2\delta_x+B_3\delta_z}\delta_x^{B_4}\delta_z^{B_5}+\\ &C_1e^{C_2\delta_x+C_3\delta_z}\delta_x^{C_4}+\\ &D_1e^{D_2\delta_x+D_3\delta_z}\delta_z^{D_4},\end{aligned} \tag{13}$$

using the same scaling as in (12). The exponential terms (all exponents are negative) assure that $\boldsymbol{F}$ and $\boldsymbol{T}$ relax to the known asymptotic/exact solutions given in (12), here denoted $\alpha_*(\delta_x)$ and $\beta_*(\delta_z)$, where $*$ denotes the force or torque to fit, e.g. $\alpha_{F_x}(\delta_x)$ refers to the asymptote along the wall $x=0$ of the force F_x. The two factors containing the polar angle θ are introduced to ensure the asymptotic/exact solutions are recovered near both walls, all along $z=0$ $(\theta=0)$ and $x=0$ $(\theta=\pi/2)$. The reader is referred to the appendix for a check of the consistency of this fit with

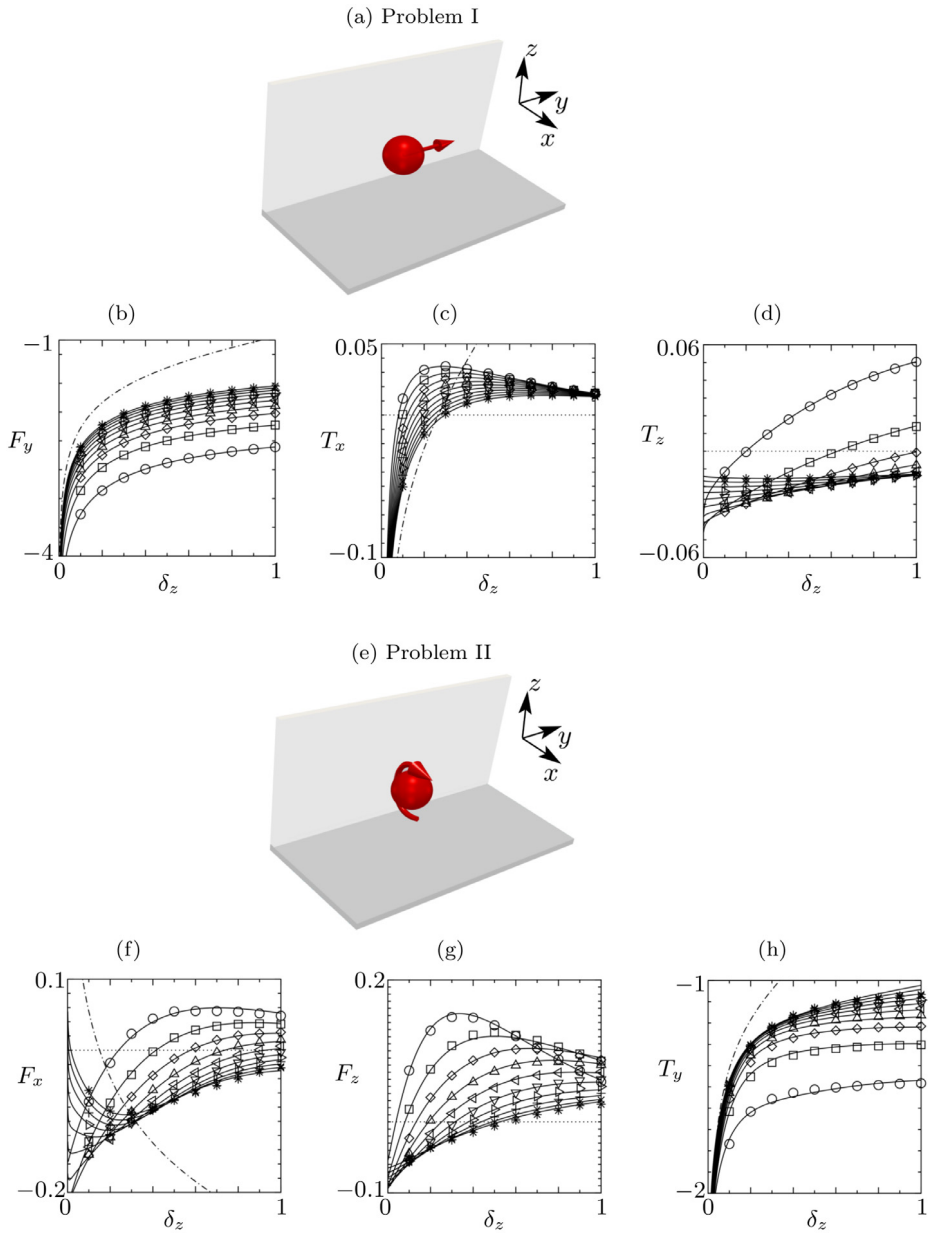

Fig. 4. Sketch of the six fundamental problems (left column) and corresponding hydrodynamic forces and torques on the particle as functions of δ_z (three right columns). The markers denote constant $\delta_x = 0.1$ (○), 0.2 (□), 0.3 (◇), 0.4 (△), 0.5 (◁), 0.6 (▽), 0.7 (▷), 0.8 (+), 0.9 (×) and 1 (∗). The fit functions (13) are represented by solid lines. Dash–dotted lines represent the asymptotes $\beta_*(\delta_z)$ and dotted lines indicate the zero level.

the asymptotic solutions. The power laws in δ_x and δ_z are typical of near-wall trends. The 17 fit coefficients A_i, B_i, C_i and D_i are determined by least-squares. They are listed in Table 2. Whenever the asymptotic solution is zero, $\alpha_*(\delta_x) = 0$ or $\beta_*(\delta_z) = 0$, the corresponding coefficients A_i are not defined. All the coefficients are computed enforcing the symmetries of the problem. An initial fitting operation is performed using all the coefficients involved in (13). If the magnitude of a coefficient is less than 10^{-4}, the least-squares fit is recomputed, enforcing that such coefficient is zero.

Depending on the elementary case considered different asymptotic limits can arise.

(I) The sphere translates (without rotation) parallel to the dihedral edge at distances δ_x and δ_z from the two stationary walls. This problem admits two limits of type (12b), represented by a sphere translating parallel to a solid wall: (i) $\boldsymbol{t}_1 = \boldsymbol{e}_y$, $\boldsymbol{t}_2 = \boldsymbol{e}_z$ and $\delta = \delta_x$, and (ii) $\boldsymbol{t}_1 = \boldsymbol{e}_y$, $\boldsymbol{t}_2 = -\boldsymbol{e}_x$ and $\delta = \delta_z$.

(II) The sphere rotates (without translation) about an axis parallel to the dihedral edge. This case admits two limits corresponding (12d) with (i) $\boldsymbol{t}_1 = -\boldsymbol{e}_z$, $\boldsymbol{t}_2 = \boldsymbol{e}_y$ and $\delta = \delta_x$, and (ii) $\boldsymbol{t}_1 = \boldsymbol{e}_x$, $\boldsymbol{t}_2 = \boldsymbol{e}_y$ and $\delta = \delta_z$.

(III) The sphere translates (without rotation) in x direction normal to one wall. This problem admits two different limits corresponding to (i) wall-normal motion (12a) with $\boldsymbol{n} = \boldsymbol{e}_x$ and $\delta = \delta_x$, and (ii) wall-tangential motion (12b) with $\boldsymbol{t}_1 = \boldsymbol{e}_x$, $\boldsymbol{t}_2 = \boldsymbol{e}_y$ and $\delta = \delta_z$. The problem is equivalent to the case when the particle translates in z direction. Forces and torque for this latter case are obtained by the transformation $(\delta_x, F_x, \delta_z, F_z, T_y) \to (\delta_z, F_z, \delta_x, F_x, -T_y)$.

(IV) The sphere rotates (without translation) about an axis perpendicular to one wall. In this case two different asymptotic limits arise: (i) a sphere rotating parallel to a wall

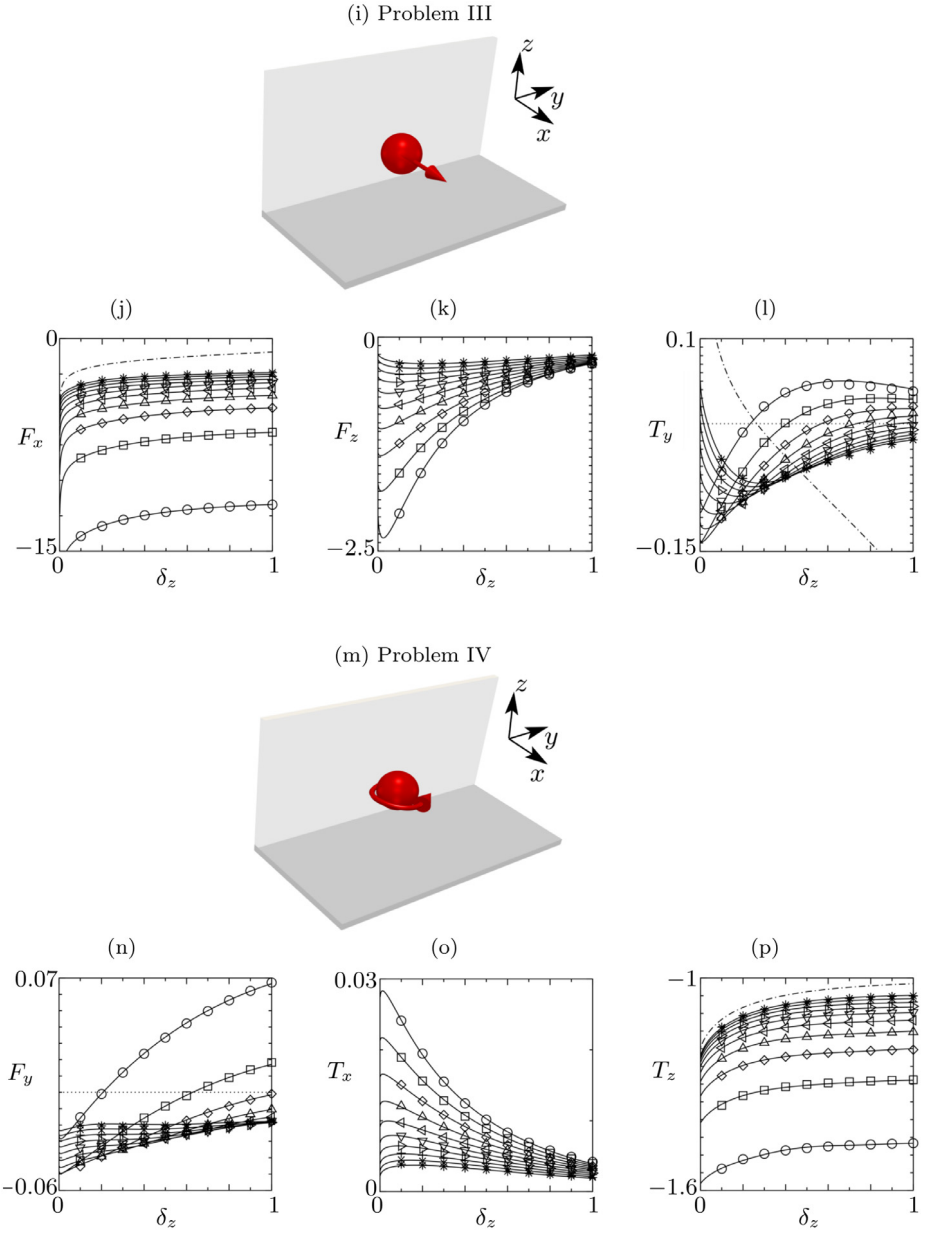

Fig. 4. (*continued*).

(12d) with the identification $\boldsymbol{t}_2 = \boldsymbol{e}_z$, $\boldsymbol{t}_1 = \boldsymbol{e}_y$ and $\delta = \delta_x$, and (ii) a sphere rotating normal to a wall (12c) with $\boldsymbol{n} = \boldsymbol{e}_z$ and $\delta = \delta_z$. As for Problem III, the force and torques for this case $\boldsymbol{\Omega} \parallel \boldsymbol{e}_z$ are mirror symmetric to the ones for $\boldsymbol{\Omega} \parallel \boldsymbol{e}_x$.

(V) A sphere is at rest near a dihedral corner formed by a stationary wall and a wall sliding parallel to the edge. Apart from the trivial limit in which both the sphere and the near wall are at rest ($\alpha_*(\delta_x) = 0$), the other asymptotic limit corresponds to (12b) (analogous to the sphere sliding tangentially to a steady wall) with the identification $\boldsymbol{t}_2 = \boldsymbol{e}_x$, $\boldsymbol{t}_1 = -\boldsymbol{e}_y$ and $\delta = \delta_z$.

(VI) A stationary sphere is located near a dihedral corner formed by a stationary wall and a wall sliding perpendicular to the edge. This problem admits the trivial limit of a steady sphere near a steady wall ($\alpha_*(\delta_x) = 0$) and the limit (12b) with the identification $\boldsymbol{t}_2 = -\boldsymbol{e}_y$, $\boldsymbol{t}_1 = -\boldsymbol{e}_x$ and $\delta = \delta_z$.

4.4. Application to the motion of a finite-size particle in a cavity

In a recent study on accumulation of particles in a two-sided lid-driven cavity, Romanò et al. [7] employed a simplified version of the Maxey–Riley equation [46] complemented by a lubrication model to take into account the particle–boundary interaction. The enhanced drag force a particle experiences when moving near a boundary was modeled using the classical lubrication expansions for a particle moving towards an infinite plane wall. The authors pointed out that using this model for the near wall motion unphysical point attractors are created, one at each of the two dihedral corners. This indicates that a mere superposition of classical particle–wall solutions cannot properly represent the particle motion near the edge.

In the following, we employ the same simplified Maxey–Riley equation as in [7] in which buoyancy forces, the Basset history term, the Saffman and the Faxén corrections are neglected, i.e.,

$$\ddot{\boldsymbol{y}} = \left(\frac{1}{\varrho + 1/2}\right)\left[-\frac{\varrho}{\mathrm{St}}\left(\dot{\boldsymbol{y}} - \boldsymbol{u}\right) + \frac{3}{2}\frac{\mathrm{D}\boldsymbol{u}}{\mathrm{D}t}\right]. \tag{14}$$

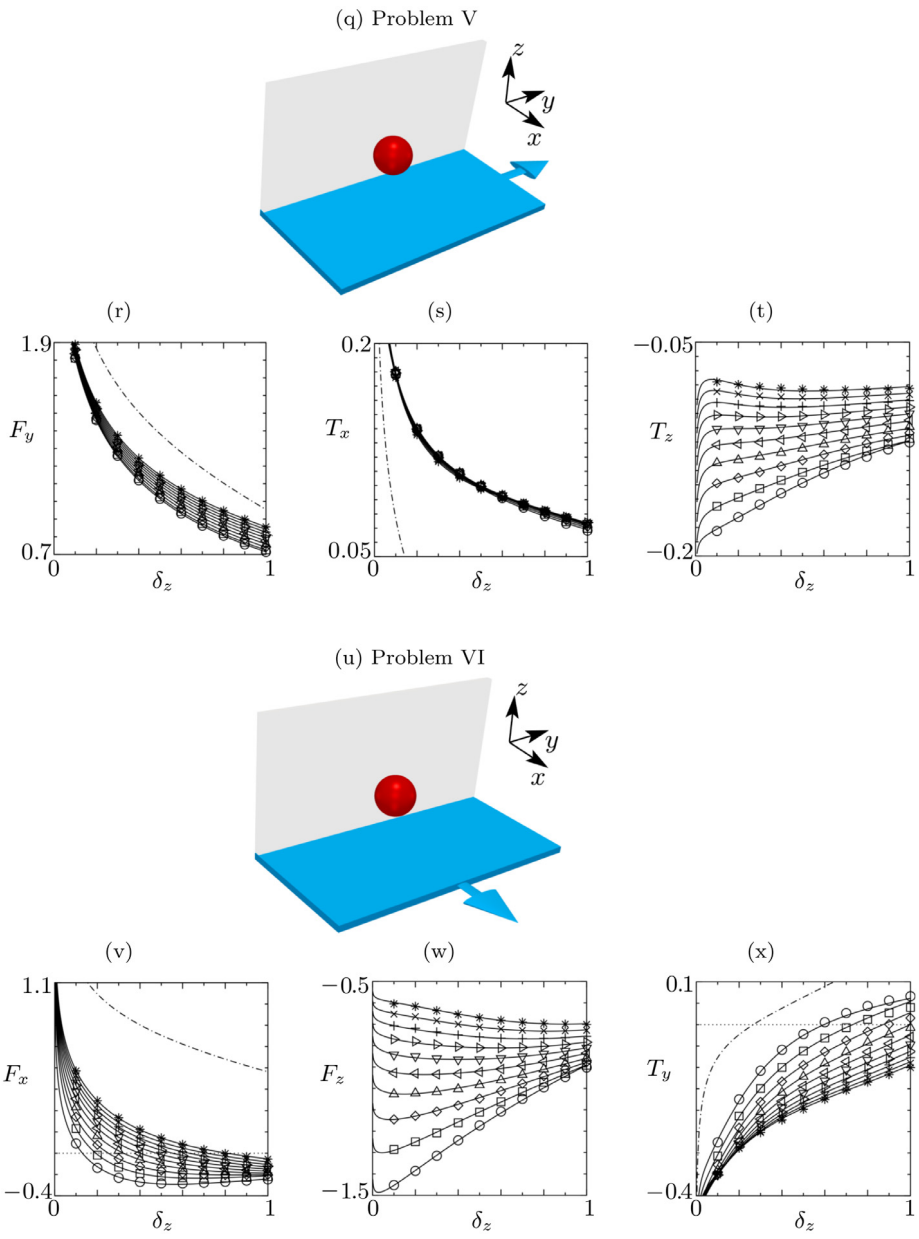

Fig. 4. (*continued*).

In (14) D/Dt represents the material derivative along a fluid flow trajectory, $\boldsymbol{y}$ denotes the position of the particle's centroid, and

$$\varrho = \frac{\rho_\mathrm{p}}{\rho} \quad \text{and} \quad \mathrm{St} = \varrho\frac{2a^2}{9H^2} \tag{15}$$

are the particle-to-fluid density ratio and Stokes number, respectively, with ρ_p the density of the particle and H the characteristic length of the flow.

To demonstrate the improvement of the particle motion model which can be achieved using the fit functions 4.3 determined numerically in Section 4.3 we consider two different particle–boundary interaction models.

Model I: In Model I the exact/asymptotic forces (12) for infinite plane boundaries are added to the right-hand-side of (14), whenever the particle moves at distance $\delta_x \leq 1$ or $\delta_z \leq 1$ from the walls.

Model II: Model II is the same as Model I, except that the superposition of the classic asymptotic/exact solutions is replaced by (13), whenever both $\delta_x \leq 1$ and $\delta_z \leq 1$.

The two models are applied to the same setup investigated in [7]: The flow is driven in a rectangular cavity with an aspect ratio $\Gamma = W/H = 1.7$, where W denotes the width in x of the cavity and H its height in y direction. The two facing walls at $x = -W/2$ and $x = W/2$ move with constant velocities $\pm V_\mathrm{w}\boldsymbol{e}_y$ in antiparallel direction. At Reynolds number $\mathrm{Re} = HV_\mathrm{w}/\nu = 400$ (as in [7]) a periodic steady cellular flow exists with wavelength $\lambda_z = 2.73\,H$ in z direction. As flow domain we consider a single rectangular cell within $z = \pm\lambda_z/4$, corresponding to half a wavelength in the z direction. For further details, we refer to [7]. The reason why finite-size particles can get trapped in the corners using (14) is the velocity vector projected onto the (x, y) plane is directed towards the corner along the lines $(x, y) = (\pm\Gamma/2 \mp a, \pm 1/2 \mp a)$, more precisely $\boldsymbol{n}_x \cdot \boldsymbol{u} > 0$ *and* $\boldsymbol{n}_y \cdot \boldsymbol{u} > 0$ along this line, where $\boldsymbol{n}_x$ and $\boldsymbol{n}_y$ are the outward normal vectors on the boundaries.

Fig. 5 depicts the indistinguishable particle configurations at $t = 1$ which result from both the models using $N = 4096$ particles with $\varrho = 1$ and $a = 0.05$, initially velocity-matched

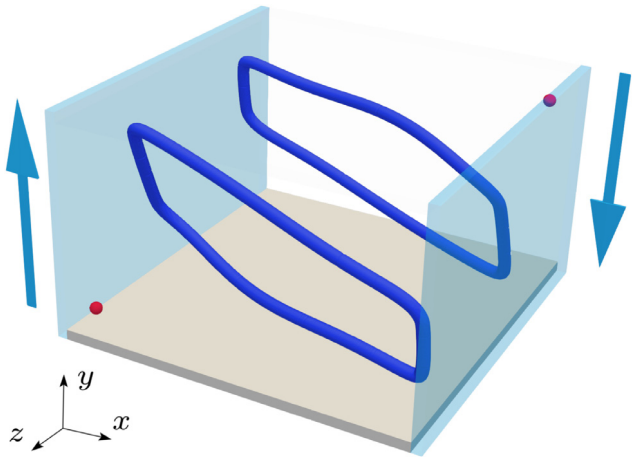

Fig. 5. Configuration of $N = 4096$ finite-size and density-matched particles at $t = 1$ (in units of H^2/ν). Particles attracted to the periodic orbit are shown in blue, whereas particles attracted to any of the two corner attractors are shown in red. The moving walls are colored in light blue. (For interpretation of the references to color in this figure legend, the reader is referred to the web version of this article.)

to the flow and randomly distributed in the subdomain $[-\Gamma/2 + a,\ \Gamma/2 - a] \times [-1/2 + a,\ 1/2 - a] \times [-\lambda_z/4,\ \lambda_z/4]$, i.e. the statically accessible volume for each particle. In both models we find the same periodic attractors (blue) and point attractors (red) in the cavity corners at $(x, y, z) = (\pm\Gamma/2 \mp a, \pm 1/2 \mp a, \mp\lambda_z/4)$. The difference among the two configurations is using Model I 861 $(0.2102 \times N)$ of the non-interacting particles have been attracted to the corners, whereas in Model II which makes use of (13) only 47 $(0.0115 \times N)$ particles end up in the corners. Thus the result of Model II is closer to the experimental findings [33,40,41] in which *all* particles are attracted to one of the two periodic orbits seen in Fig. 5.

We observe only particles initialized very close to a stationary wall become trapped in one of the corner attractors. To more accurately characterize the basin of attraction of the corner attractors, 10,000 particles were initialized randomly and velocity matched in the shallow cuboidal volume $[-\Gamma/2 + a,\ \Gamma/2 - a] \times [-1/2 + a,\ -1/2 + 1/10] \times [-\lambda_z/4,\ \lambda_z/4]$. Fig. 6 shows the initial state in which particles are color coded according to their attractors. Particles which become attracted to $(x, y, z) = (-\Gamma/2 + a, -1/2 + a, \lambda_z/4)$ are shown in red, while those being attracted to the periodic attractors have a gray color. Only particles from a very thin layer near the solid wall upstream of the respective moving wall are attracted to the corner attractor. The thickness of the layer depends on the (x, z) coordinates and has a structure in z direction which results of the three-dimensionality of the flow. The layer of red particles on the solid wall shown does not seem to extend to the corner at $(x, y) = (\Gamma/2, -1/2)$. Therefore, the red particles are directly attracted to the corner $(x, y) = (-\Gamma/2, -1/2)$ and do not circulate in the cavity. The attraction to the corners of near-wall particles in our models, as opposed to the experimental evidence, is most likely due to the lack of second-order effects which could lift up particles from the walls [47,48].

A more quantitative analysis of the different dynamics of Model I and Model II is presented in Fig. 7 by displaying the fraction of particles $n(t)/N$ which is attracted to any of the periodic (blue lines) or the point attractors (red lines). A particle is considered attracted if the distance of its centroid from one of the periodic or from one of the corner attractors is less than $a/2$. It can be seen that the fraction of particles attracted to the corner attractors (red) is significantly less for Model II (solid lines) as compared to Model I (dashed lines). Moreover, the initial evolution of the fraction of particles attracted to the periodic attractors (blue) is similar. However, from about $t \approx 0.1$ the fraction of particles attracted to the periodic orbits increases more rapidly for Model II, because more particles remain available for the periodic attractors than in Model I. The initial attraction to the corner attractors (red), in particular for Model I (dashed lines), is more rapid than for the periodic attractors, because those near-wall particles directly move to the edges from where they slide to the cell boundaries at $z = \pm\lambda_z/4$, see Figs. 5 and 6.

Finally, the periodic attractors existing in both models are capable of reproducing the experimental results. Fig. 8 shows a snapshot at $t = 3$ of 4049 particles (out of 4096) attracted to the periodic attractor using Model II (blue). The attractor agrees very well with the experimental particle configuration (turquoise) [33], despite of the slight geometrical differences between the experimental ($\Gamma = 1.6$, curved driving walls) and the numerical geometry ($\Gamma = 1.7$, straight driving walls).

5. Discussion and conclusion

The general Stokesian motion of a sphere near a semi-infinite dihedral corner has been considered. The solution can be obtained by superposition of six elementary types of motion according to the components of the velocity $\boldsymbol{U}$ and rotation rate vector $\boldsymbol{\Omega}$ of the sphere. Forces $\boldsymbol{F}$ and torques $\boldsymbol{T}$ on the sphere were quantified by numerically solving the six problems of complementary fundamental motions. For all fundamental cases robust fits of the data have been proposed, which take into account all symmetries

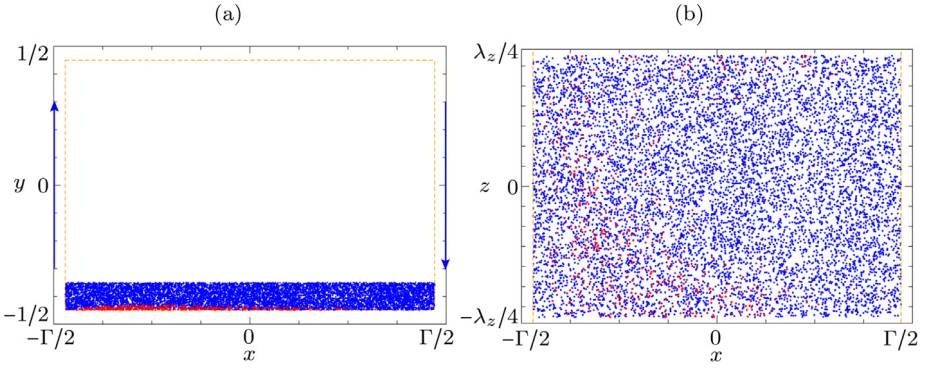

Fig. 6. Random initial positions of $N = 10000$ velocity-matched particles in the layer $[-\Gamma/2 + a,\ \Gamma/2 - a] \times [-1/2 + a,\ -1/2 + 1/10] \times [-\lambda_z/4,\ \lambda_z/4]$. Red dots indicate the centroids of particle attracted to the bottom left corner. Blue dots represent centroids of particles attracted to periodic orbits. (a) Projection to the (x, y) plane, (b) projection to the (x, z) plane. The blue arrows in (a) denote the antiparallel motion of the cavity lids. (For interpretation of the references to color in this figure legend, the reader is referred to the web version of this article.)

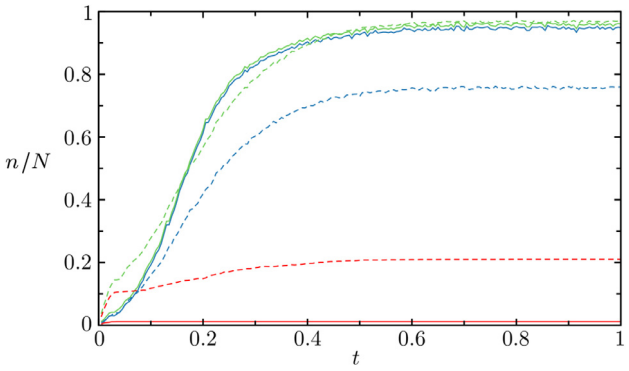

Fig. 7. Fraction of particles $n(t)/N$ attracted to one of the periodic attractors (blue lines) or to one of the corner attractors (red lines) as functions of time in units of the viscous diffusion time. The total fraction of particles attracted to any attractor is indicated by green lines. Results are shown for Model I (dashed lines) and for Model II (full lines). All $N = 4096$ particles have radius $a = 0.05$ and are density-matched to the fluid. They are initialized at $t = 0$ velocity-matched to the flow and randomly distributed in $[-\Gamma/2+a,\ \Gamma/2-a]\times[-1/2+a,\ 1/2-a]\times[-\lambda_z/4,\ \lambda_z/4]$. (For interpretation of the references to color in this figure legend, the reader is referred to the web version of this article.)

of the problem, all exact solutions, and all asymptotic solutions derived by lubrication theory for a particle moving near a wall. The fits provided in (13) are valid near an edge within the range $(x, z) = (1 + \delta_x, 1 + \delta_z) = (h_x, h_z)/a = \mathcal{O}(1)$ for the position of the centroid. Since the known solutions for a particle near a wall are incorporated in the fit, we expect (13) to be applicable even for $\delta_x + \delta_z \gg 1$, as long as the classical lubrication approximation holds, i.e. as long as $\delta_x \ll 1$ with $\delta_z \gg 1$, or $\delta_x \gg 1$ with $\delta_z \ll 1$.

A solution to the Navier–Stokes problem for the motion of a finite-size particle near a dihedral corner would require the accurate resolution of the flow fields on all scales involved in the problem, i.e. on the large scale of the fluid flow, over the particle scale, and down to the scale of the lubrication gap. Treating this problem in the limit of creeping flow restricts the Reynolds numbers of the flow and of the particle for which the approximation is valid. On the other hand, considering the creeping flow regime allows to exploit the superposition principle for linear problems. As a result, the dimension of the phase space of the problem is significantly reduced, memory effects do not need to be taken into account, and non-linear interactions between the six fundamental motions identified in this paper do not arise. Moreover, owing to the instantaneous character of the Stokes equations, numerical simulations can be carried out on a stationary grid. In terms of computational resources, this approach makes possible the large parametric study carried out and allows for a fit that only depends on the relative position of the particle with respect to the corner, on the particle and the sliding wall velocities.

The fit of the forces and torques has been constructed as to match with asymptotic solutions derived by lubrication theory for plane walls. This extends the range of validity of the fit beyond the immediate vicinity of the corner. In fact, far away from the corner, the particle is supposed to be affected only by the presence of the nearest solid wall, when the separation distance δ is small. The fit of the forces and torques proposed well converges to the theoretical asymptotes already at a distance much shorter than 100 particle radii from the corner. Moreover, far away from the boundaries the Maxey–Riley equation is already consistent with the creeping flow approximation. Therefore, the motion of a sphere in creeping flow can well be captured supplying the Maxey–Riley equation with our fit, as realized in Model II. We stress, however, that creeping-flow models such as the Maxey–Riley equation and the Stokesian lubrication model, are widely used in literature even beyond their range of validity, i.e. for non-vanishing particle Reynolds numbers. Indeed, inertial effects become important when the particle Reynolds number is of order 10 or higher, as also demonstrated by weakly-inertial lubrication theory [26] and finite-Reynolds Saffman-lift effects.

Dealing with a wedge by simply superposing the asymptotic solutions for two plane walls is conceptually not always correct. This approach was used by Brenner [13], even though he pointed out that a superposition of classical asymptotic solutions may be permissible only if the distance from the edge is sufficiently large, while the particle is close to one of the walls. When $\delta_x \to 0$ and δ_z is large enough, or viceversa, the asymptotic solutions are recovered. However, in the dedicated limit $\delta_x \to 0$ and $\delta_z \to 0$, with $\lim_{(\delta_x,\delta_z)\to(0,0)} \delta_x/\delta_z = \mathcal{O}(1)$, leading-order lift forces and torques arise due to a non-linear confinement effect, which cannot be taken into account by a linear superposition of asymptotic lubrication-type of solutions for a sphere moving close to an infinite plane wall, as also demonstrated by Romanò et al. [7]. For instance, the non-monotonous dependence of the torque T_y in case III (Fig. 4l) is a result of opposing contributions: The positive torque induced by the wall at $z = 0$ when $\delta_z \to 0$ (see dashed–dotted line for the asymptotic solution) might be opposed by a negative contribution to the torque as a result of the confinement effect created by the wall at $x = 0$. This behavior cannot be represented by the two asymptotic solutions near plane walls corresponding to the two limits $(\delta_x \to \infty, \delta_z \to 0)$ and $(\delta_x \to 0, \delta_z \to \infty)$. In the latter limit $T_y(\delta_x \to 0, \delta_z \to \infty) \to 0$.

The usefulness of the fit functions (13) is demonstrated by reducing the number of particles attracted to the spurious attractors by a factor 20 when using Model II as compared to Model I. The remaining small fraction of near-wall initial conditions

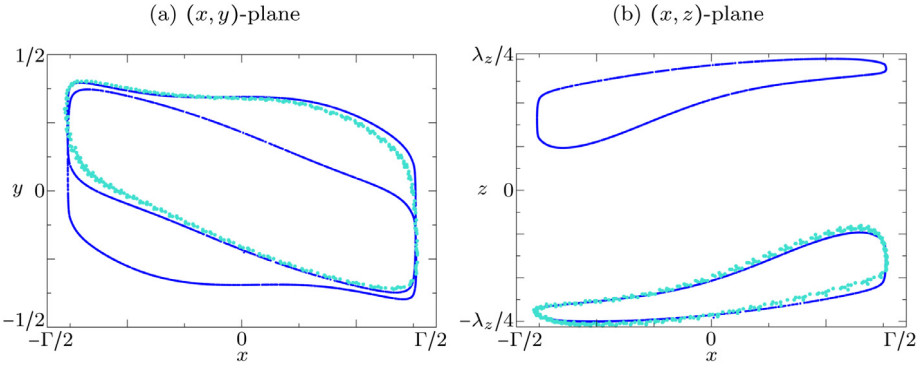

Fig. 8. Snapshot at $t = 3$ of 4049 particles (out of 4096) using Model II (blue). The experimental result (turquoise) was obtained by particle tracking [33]. (a) Projection onto the (x, y) plane; (b) projection onto the (x, z) plane. (For interpretation of the references to color in this figure legend, the reader is referred to the web version of this article.)

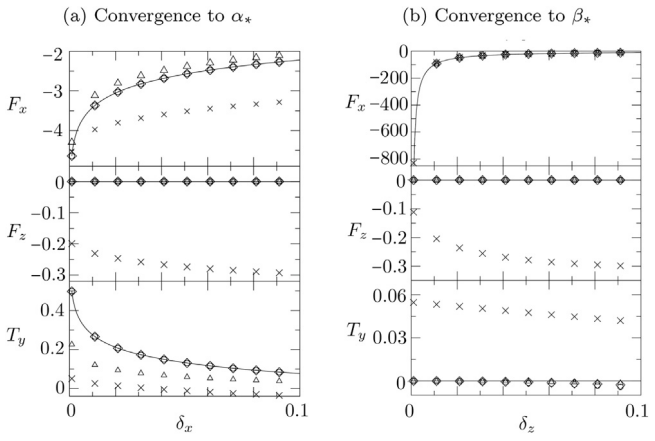

Fig. 9. Comparison between the fit (13) and the asymptotic solutions (12) for case III. The lubrication solutions α_* and β_* for small δ_x and δ_z, respectively, are indicated by lines. Symbols in (a) denote $\delta_z = 1$ (×), 10 (△), 100 (◇), and 1000 (○). Symbols in (b) denote $\delta_x = 1$ (×), 10 (△), 100 (◇), and 1000 (○). (For interpretation of the references to color in this figure legend, the reader is referred to the web version of this article.)

for which particles cannot escape the corners might vanish if higher-order corrections and inertial effects are taken into account. These corrections are not taken care of in our model, but they are probably required for simulating flows at moderate Reynolds numbers. Nevertheless, most of the limitations imposed by the use of linear superposition of classic lubrication results are overcome by our creeping flow model, which is also in good agreement with the experimental data of [33]. The accuracy of our simulations, on which the fit functions are based, candidates our results to be benchmark-quality data for further numerical studies. The accuracy of the data is confirmed by correctly retrieving the restrictions imposed by the reciprocal theorem, i.e. $F^*F_y(\text{case IV}) = T^*T_z(\text{case I})$ and $F^*F_x(\text{case II}) = T^*T_y(\text{case III})$.

Beyond the interest in the specific flow problem, we expect our results to contribute to the development of sub-grid-scale models for particulate numerical simulations which take into account non-linear effects important, e.g., when a particle moves in a rectangular duct or in long cavities, far from a trihedral corner. When a particle is transported close to a boundary such that the numerical grid resolution is insufficient to accurately represent the flow field in the lubrication gap between particle and wall, lubrication-force (by far dominant at small δ) models can be employed near a wall. Alternatively, in case of edges, the present fit can be used. The same approach has been used by [49], who included a particle–boundary modeling layer for the simulations of particle-laden flow. Finally, the proposed fits might guide subsequent asymptotic analyses, which could include the confinement effect due to the corner, extending the near-wall to near-edge asymptotic solutions.

Declaration of competing interest

The authors declare that they have no known competing financial interests or personal relationships that could have appeared to influence the work reported in this paper.

Appendix

The convergence of the fit (13) to the classic asymptotic solutions for $(\delta_x, \delta_z) \to (0, \infty)$ and $(\delta_x, \delta_z) \to (\infty, 0)$ has been verified for all forces and torques of all six cases presented in our study. As an example we consider problem III, a sphere translating in x-direction. Fig. 9 shows the lubrication functions α_* and β_* (solid lines) for small δ_x and δ_z, respectively. All symbols indicate the present fit functions. As can be seen, far enough from the corner, i.e. for $\delta_x + \delta_z > 10$, the fit (13) converges to the known asymptotic solutions in the range of validity of such asymptote, i.e. $\delta_x \to 0$ for α_* and $\delta_z \to 0$ for β_*.

References

[1] K.W. Nicholson, A review of particle resuspension, Atmos. Environ. 22 (12) (1988) 2639–2651.
[2] E.D. Andrews, Entrainment of gravel from naturally sorted riverbed material, GSA Bull. 94 (10) (1983) 1225–1231.
[3] A. Džiugys, B. Peters, An approach to simulate the motion of spherical and non-spherical fuel particles in combustion chambers, Granul. Matter 3 (4) (2001) 231–266.
[4] D. Schwabe, A.I. Mizev, M. Udhayasankar, S. Tanaka, Formation of dynamic particle accumulation structures in oscillatory thermocapillary flow in liquid bridges, Phys. Fluids 19 (7) (2007) 072102.
[5] M. Orlishausen, L. Butzhammer, D. Schlotbohm, D. Zapf, W. Köhler, Particle accumulation and depletion in a microfluidic Marangoni flow, Soft Matter 13 (39) (2017) 7053–7060.
[6] F. Romanò, H.C. Kuhlmann, Finite-size Lagrangian coherent structures in thermocapillary liquid bridges, Phys. Rev. Fluids 3 (9) (2018) 094302.
[7] F. Romanò, P. Kunchi Kannan, H.C. Kuhlmann, Finite-size Lagrangian coherent structures in a two-sided lid-driven cavity, Phys. Rev. Fluids 4 (2) (2019) 024302.
[8] H.A. Lorentz, Ein allgemeiner Satz, die Bewegung einer reibenden Flüssigkeit betreffend, nebst einigen Anwendungen desselben, Abh. Theor. Phys. 1 (1907) 23–42.
[9] G.B. Jeffery, On the steady rotation of a solid of revolution in a viscous fluid, Proc. Lond. Math. Soc. 2 (1) (1915) 327–338.
[10] M. Stimson, G.B. Jeffery, The motion of two spheres in a viscous fluid, Proc. R. Soc. Lond. Ser. A Math. Phys. Eng. Sci. 111 (757) (1926) 110–116.
[11] D. Papavassiliou, G.P. Alexander, Exact solutions for hydrodynamic interactions of two squirming spheres, J. Fluid Mech. 813 (2017) 618–646.
[12] H. Faxén, Die Geschwindigkeit zweier Kugeln, die unter Einwirkung der Schwere in einer zähen Flüssigkeit fallen, Z. Angew. Math. Mech. 7 (1) (1927) 79–80.
[13] H. Brenner, The slow motion of a sphere through a viscous fluid towards a plane surface, Chem. Eng. Sci. 16 (3–4) (1961) 242–251.
[14] W.R. Dean, M.E. O'Neill, A slow motion of viscous liquid caused by the rotation of a solid sphere, Mathematika 10 (1) (1963) 13–24.
[15] M.E. O'Neill, K. Stewartson, On the slow motion of a sphere parallel to a nearby plane wall, J. Fluid Mech. 27 (4) (1967) 705–724.
[16] A. Goldman, R. Cox, H. Brenner, Slow viscous motion of a sphere parallel to a plane wall: I Motion through a quiescent fluid, Chem. Eng. Sci. 22 (4) (1967) 637–651.
[17] A. Goldman, R. Cox, H. Brenner, Slow viscous motion of a sphere parallel to a plane wall: II Couette flow, Chem. Eng. Sci. 22 (4) (1967) 653–660.
[18] W.L. Haberman, R.M. Sayre, Motion of rigid and fluid spheres in stationary and moving liquids inside cylindrical tubes, 1958, David Taylor Model Basin Report No. 1143.
[19] R.M. Sonshine, R.G. Cox, H. Brenner, The Stokes translation of a particle of arbitrary shape along the axis of a circular cylinder, Appl. Sci. Res. 16 (1) (1966) 325–360.
[20] R.G. Cox, H. Brenner, The slow motion of a sphere through a viscous fluid towards a plane surface: II Small gap widths, including inertial effects, Chem. Eng. Sci. 22 (12) (1967) 1753–1777.
[21] E. Bart, The slow unsteady settling of a fluid sphere toward a flat fluid interface, Chem. Eng. Sci. 23 (3) (1968) 193–210.
[22] S.H. Lee, L.G. Leal, Motion of a sphere in the presence of a plane interface. Part 2. An exact solution in bipolar co-ordinates, J. Fluid Mech. 98 (1) (1980) 193–224.
[23] A.S. Geller, S.H. Lee, L.G. Leal, The creeping motion of a spherical particle normal to a deformable interface, J. Fluid Mech. 169 (1986) 27–69.
[24] C.L. Darabaner, S.G. Mason, Particle motions in sheared suspensions XXII: Interactions of rigid spheres (experimental), Rheol. Acta 6 (3) (1967) 273–284.
[25] J. Happel, H. Brenner, Low Reynolds Number Hydrodynamics: with Special Applications to Particulate Media, Vol. 1, Springer Science & Business Media, 2012.
[26] R.G. Cox, S.G. Mason, Suspended particles in fluid flow through tubes, Ann. Rev. Fluid Mech. 3 (1) (1971) 291–316.
[27] Q. Liu, A. Prosperetti, Wall effects on a rotating sphere, J. Fluid Mech. 657 (2010) 1–21.
[28] S. Kim, W. Russel, The hydrodynamic interactions between two spheres in a Brinkman medium, J. Fluid Mech. 154 (1985) 253–268.
[29] E.R. Damiano, D.S. Long, F.H. El-Khatib, T.M. Stace, On the motion of a sphere in a Stokes flow parallel to a Brinkman half-space, J. Fluid Mech. 500 (2004) 75–101.

[30] F. Romanò, H.C. Kuhlmann, Numerical investigation of the interaction of a finite-size particle with a tangentially moving boundary, Int. J. Heat Fluid Flow 62 Part A (2016) 75–82.
[31] F. Romanò, H.C. Kuhlmann, Particle–boundary interaction in a shear-driven cavity flow, Theor. Comput. Fluid Dyn. 31 (2017) 427–445.
[32] F. Romanò, H.C. Kuhlmann, M. Ishimura, I. Ueno, Limit cycles for the motion of finite-size particles in axisymmetric thermocapillary flows in liquid bridges, Phys. Fluids 29 (9) (2017) 093303.
[33] F. Romanò, H. Wu, H.C. Kuhlmann, A generic mechanism for finite-size coherent particle structures, Int. J. Multiph. Flow. 111 (2019) 42–52.
[34] D. Schwabe, P. Hintz, S. Frank, New features of thermocapillary convection in floating zones revealed by tracer particle accumulation structures (PAS), Microgravity Sci. Technol. 9 (1996) 163–168.
[35] E. Hofmann, H.C. Kuhlmann, Particle accumulation on periodic orbits by repeated free surface collisions, Phys. Fluids 23 (2011) 0721106.
[36] R.V. Mukin, H.C. Kuhlmann, Topology of hydrothermal waves in liquid bridges and dissipative structures of transported particles, Phys. Rev. E 88 (2013) 053016–1–053016–20.
[37] F.H. Muldoon, H.C. Kuhlmann, Coherent particulate structures by boundary interaction of small particles in confined periodic flows, Physica D 253 (2013) 40–65.
[38] I. Barmak, F. Romanò, H.C. Kuhlmann, Particle accumulation in high-Prandtl-number liquid bridges, Proc. Appl. Math. Mech. 19 (2019) e201900058.
[39] F. Romanò, H.C. Kuhlmann, Finite-size coherent structures in thermocapillary liquid bridges: A review, Int. J. Microgravity Sci. Appl. 36 (2019) 360201–1–360201–17.
[40] H.C. Kuhlmann, F. Romanò, H. Wu, S. Albensoeder, Particle-motion attractors due to particle-boundary interaction in incompressible steady three-dimensional flows, in: G. Ivey, T. Zhou, N. Jones, S. Draper (Eds.), The 20th Australasian Fluid Mechanics Conference, Australasian Fluid Mechanics Society, 2016, p. 102, Paper no. 449.
[41] H. Wu, F. Romanò, H.C. Kuhlmann, Attractors for the motion of finite-size particles in a two-sided lid-driven cavity, in: PAMM, Vol. 17, GAMM, 2017, pp. 669–670.
[42] J. Dauparas, E. Lauga, Leading-order Stokes flows near a corner, IMA J. Appl. Math. 83 (4) (2018) 590–633.
[43] C. Kuehn, F. Romanò, H.C. Kuhlmann, Tracking particles in flows near invariant manifolds via balance functions, Nonlinear Dynam. 92 (3) (2018) 983–1000.
[44] G.I. Taylor, On scraping viscous fluid from a plane surface, in: Miszellaneen der Angewandten Mechanik, 1962, pp. 313–315.
[45] M. Chaoui, F. Feuillebois, Creeping flow around a sphere in a shear flow close to a wall, Q. J. Mech. Appl. Math. 56 (3) (2003) 381–410.
[46] M.R. Maxey, J.J. Riley, Equation of motion for a small rigid sphere in a nonuniform flow, Phys. Fluids 26 (1983) 883–889.
[47] N. Ekanayake, J.D. Berry, A.D. Stickland, D.E. Dunstan, I.L. Muir, S.K. Dower, D.J. Harvie, Lift and drag forces acting on a particle moving with zero slip velocity near a wall, 2020, arXiv preprint arXiv:2002.06142.
[48] P. Shi, R. Rzehak, Lift forces on solid spherical particles in wall-bounded flows, Chem. Eng. Sci. 211 (2019) 115264.
[49] W.-P. Breugem, A combined soft-sphere collision / immersed boundary method for resolved simulations of particulate flows, in: Proceedings of the ASME 2010, ASME, Montreal, Canada, 2010, pp. FEDSM–ICNMM2010–30634.